PHYSICAL REVIEW MATERIALS **8**, 094802 (2024)

T_c and resistivity variation induced by external bending strain in flexible film of strain-sensitive $(La, Sr)_2CuO_4$

Tomoya Horide,[1,2] Tomoaki Maekawa,[2] Tatsuro Aikawa,[3] Takanori Kitamura,[2] and Kazuma Nakamura[3,4]
[1]*Department of Electrical Engineering, Nagoya University, Furo-cho, Chikusa, Nagoya 464-8603, Japan*
[2]*Department of Materials Science and Engineering, Kyushu Institute of Technology, Kitakyushu, Fukuoka 804-8550, Japan*
[3]*Graduate School of Engineering, Kyushu Institute of Technology, 1-1 Sensui-cho, Tobata-ku, Kitakyushu, Fukuoka 804-8550, Japan*
[4]*Integrated Research Center for Energy and Environment Advanced Technology, Kyushu Institute of Technology, 1-1 Sensui-cho, Tobata-ku, Kitakyushu, Fukuoka 804-8550, Japan*

(Received 16 May 2024; accepted 9 August 2024; published 12 September 2024)

Strain in materials changes their electronic structure, and the strain response realizes rich material properties and devices. Superconductivity under hydrostatic pressure and epitaxial strain suggests significant response to an external variable strain in a single sample, but this has not yet been demonstrated because the strain is usually a fixed parameter after sample fabrication. $(La, Sr)_2CuO_4$ films were fabricated on flexible metal substrates, and bending strain was applied to them to observe the critical temperature (T_c) and resistivity variation induced by strain. The compressive bending strain of -0.005 increased the T_c from 23.4 to 27.3 K. The magnitude of the T_c change by the bending strain is independent of the doping level and initial epitaxial strain. Furthermore, the irreversibility temperature was also improved by the compressive bending, and reasonable T_c variation with respect to the reversible strain was observed. *Ab initio* density functional calculation for the mother compound La_2CuO_4 clarified that the low-energy electronic structures are sensitive to the bending strain. While the carriers (holes) are preferentially injected into the in-plane orbitals of the CuO_2 plane under the compressive strain, the tensile strain leads to the carrier injection into the perpendicular orbitals which is unfavorable to the superconductivity. The strain-sensitive high-T_c superconductor under the external strain highlights a new aspect for cuprate superconductors, which opens monitoring of the stress situation in the cryogenic systems such as superconducting magnet and liquid hydrogen container.

DOI: 10.1103/PhysRevMaterials.8.094802

I. INTRODUCTION

The response of material properties to external fields leads to rich material properties and output/conversion devices on information and energy, and much effort has been devoted to controlling this phenomenon. While electric and magnetic fields are one of the most important external fields in the recent electronics [1,2], stress and strain are becoming increasingly important for mechanical, robotic, and biological sensors [3,4]. The piezoresistive effect changes the resistivity when strain is applied, which can be used for mechanical sensing. The piezoresistive effects in metals and semiconductors are explained by the geometrical effect and band structure, which means that the piezoresistive effect has been investigated mainly for the simple physical phenomena [5]. Recently, strain has started to be applied to control the complicated phenomena in antiferromagnets [6,7], two-dimensional semiconductors [8], and quantum wells [9].

Superconductivity is one of the most interesting and physically rich phenomena. Temperature and magnetic field are dominant for the superconducting phase transition. Superconductivity is maintained at temperatures lower than the critical current (T_c) and the magnetic field lower than the upper critical field (H_{c2}) (in the case of type II superconductors). Superconductivity is also broken by high current density whose limit is defined as critical current density (J_c). Therefore, the appearance of the superconducting phase and the performance of superconducting materials are usually discussed in terms of the triple axes of temperature, magnetic field, and current density [10]. In addition, the carrier concentration can be tuned by electric field to vary the T_c [11]. Although the carrier concentration is usually assumed to be fixed after sample fabrication, electrostatic doping with electric field has successfully varied the carrier concentration and T_c. However, the T_c variation is limited to a very thin region near the surface [12–14].

T_c is also changed by the pressure effect [15–17] and film strain [18–20]. The hydrostatic pressure increases the T_c in the Hg-based superconductor from 135 to 164 K [15]. Thus, the strain can greatly change the T_c at the bulk scale. However, the hydrostatic pressure is difficult to use for device application, and the hydrostatic pressure studies focus on the fundamental interests to explore higher-T_c materials. The strain effects in films have been widely discussed for the electronic structure [21,22], oxygen content [23], and phase stability [24] in various films, and the epitaxial strain has also varied the T_c in $(La, Sr)_2CuO_4$ (LSCO) from 25 to 50 K [18]. The epitaxial strain, which is not changed after sample fabrication, also cannot be used for dynamic response to strain in devices. However, the effects of hydrostatic pressure and epitaxial strain in high-T_c superconductors suggest possible response to external strain. The mechanical properties of $YBa_2Cu_3O_y$ (YBCO) coated conductors have been investigated for commercial superconducting tapes for power and energy applications which require large current under mechanical stress [25]. More strain-sensitive high-T_c superconductors are expected to exhibit significant strain-induced variation of resistivity and T_c, which is applicable to sensor devices.

In this study, the LSCO films were fabricated on the metal substrate to observe the T_c and resistivity variation induced by the external bending strain. Here, the ion beam assisted deposition (IBAD) substrates were used as the substrate for bending the superconducting films. Although the T_c under the bending strain has been measured in the commercial YBCO tapes on the IBAD substrates, the T_c variation in YBCO is very small [26]. However, if we choose LSCO which is more sensitive to the strain, more significant output (T_c variation) is expected. For the design and understanding of the T_c variation under the external strain, the multiband electronic structure of LSCO was analyzed using density-functional theory (DFT) calculation. Based on the results, the T_c variation induced by external strain is demonstrated as an important aspect in the high-T_c superconducting properties.

II. EXPERIMENTAL AND CALCULATION DETAILS

A. Sample preparation

The LSCO films were fabricated using pulsed laser deposition (PLD) with the fourth harmonic generation of a NdYAG laser (wavelength = 266 nm). The deposition temperature, oxygen partial pressure, and substrate-target distance were 840 °C, 26 Pa, and 4 cm, respectively. The substrate was an IBAD substrate consisting of an $LaMnO_3$ top layer, an IBAD-MgO template, and a 40-μm-thick Hastelloy. The thickness of LSCO was 70–190 nm, and the Sr content, x in $(La_{1-x}, Sr_x)_2CuO_4$, was 0.1–0.25. Gold electrodes were deposited using sputtering before the T_c measurement.

B. Sample evaluation

X-ray diffraction (XRD) was used to evaluate the phase formation, lattice parameter, and orientation. The c-axis oriented LSCO films were obtained. Fourfold symmetric ϕ scan results were obtained for LSCO(103), indicating that LSCO exhibits the epitaxial relationship on the IBAD.

Resistivity-temperature (ρ-T) curves were measured using the four-probe method at a current of 0.01 mA in a physical property measurement system (Quantum Design Inc.). The voltage electrode was separated by ~1 mm and the sample width was ~2.5 mm. The thickness was 70–190 nm. The ρ-T curves were also measured for magnetic fields of 1–9 T. To investigate the influence of the bending strain on the ρ-T curves, the films were placed on the Cu bending die with the curvature radii of 9, 7, 6, 5, and 4 mm. While the convex bending results in the tensile strain, the concave bending results in the compressive strain.

C. Calculation details

In the present study, we consider three-type configurations according to the experimental situation, which is schematically shown in Fig. 1. The panels (a), (b), and (c) represent compressively bent, not-distorted (unbent), and tensile-bent configurations, respectively.

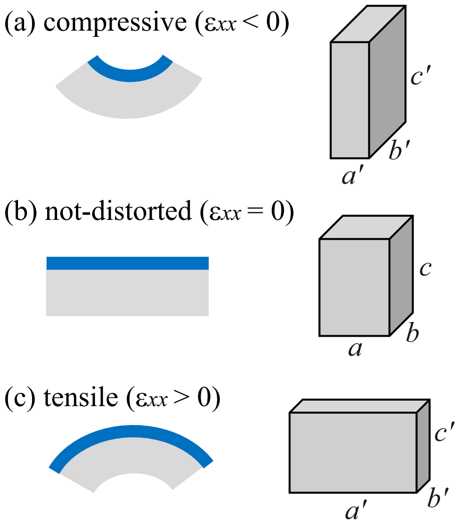

FIG. 1. Schematic figure of strained configurations and corresponding unit cell: (a) compressively bent, (b) not-distorted (unbent), and (c) tensile-bent structures. Left panels show the schematics of strained samples, and right panels show deformed unit cells with strain ε_{xx}.

When a compressive stress is applied to a sample [left of panel (a)], a tetragonal structure is distorted along the a direction [right of (a)]; its lattice parameters are changed to $a' = a(1 + \varepsilon_{xx})$, $b' = a(1-\nu\varepsilon_{xx})$, and $c' = c(1-\nu\varepsilon_{xx})$, where a and c are lattice parameters of a not-distorted structure, and the ε_{xx} is a strain along the x direction, and is negative in the compressive case. The ν is Poisson's ratio depending on the materials, and we employed $\nu = 0.3$ in this study. Thus, the compressively strained, not-distorted, and tensile-strained structures are the structures corresponding to the $\varepsilon_{xx} < 0$, $\varepsilon_{xx} = 0$, and $\varepsilon_{xx} > 0$ cases, respectively.

We performed *ab initio* density-functional calculations using Quantum ESPRESSO [27,28], where we employed norm-conserving pseudopotentials [29,30], and the generalized-gradient approximation for exchange-correlation energy proposed by Perdew, Burke, and Ernzerhof [31]. The cutoff energy for the wave function and charge density are 120 and 1200 Ry, respectively, and a Monkhorst-Pack k grid of $20 \times 20 \times 20$ was employed. The crystal structure was fully optimized so that the force on each ion and lattice parameters were less than 0.001 a.u. and 0.5 kbar, respectively. The resulting lattice constants are $a = 3.814$ Å and $c = 13.197$ Å, and this relaxed structure is corresponding to a not-distorted structure of $\varepsilon_{xx} = 0$. In the present study, we generated strained structures with $\varepsilon_{xx} = -0.1,\ -0.05,\ 0.05,$ and 0.1. For the strained lattices, we checked optimization effects of atomic configurations, but the effect seems to be small (Fig. S1 [32]). Then, in the present study, we used not-relaxed results for the discussions.

We also performed the Wannier analysis using RESPACK [34], where maximally localized Wannier functions for all the Cu-d and O-p orbitals were constructed. In La_2CuO_4, since the bands involving the Cu-d and O-p orbitals are well isolated from other bands (see Fig. S2 [32]), we constructed

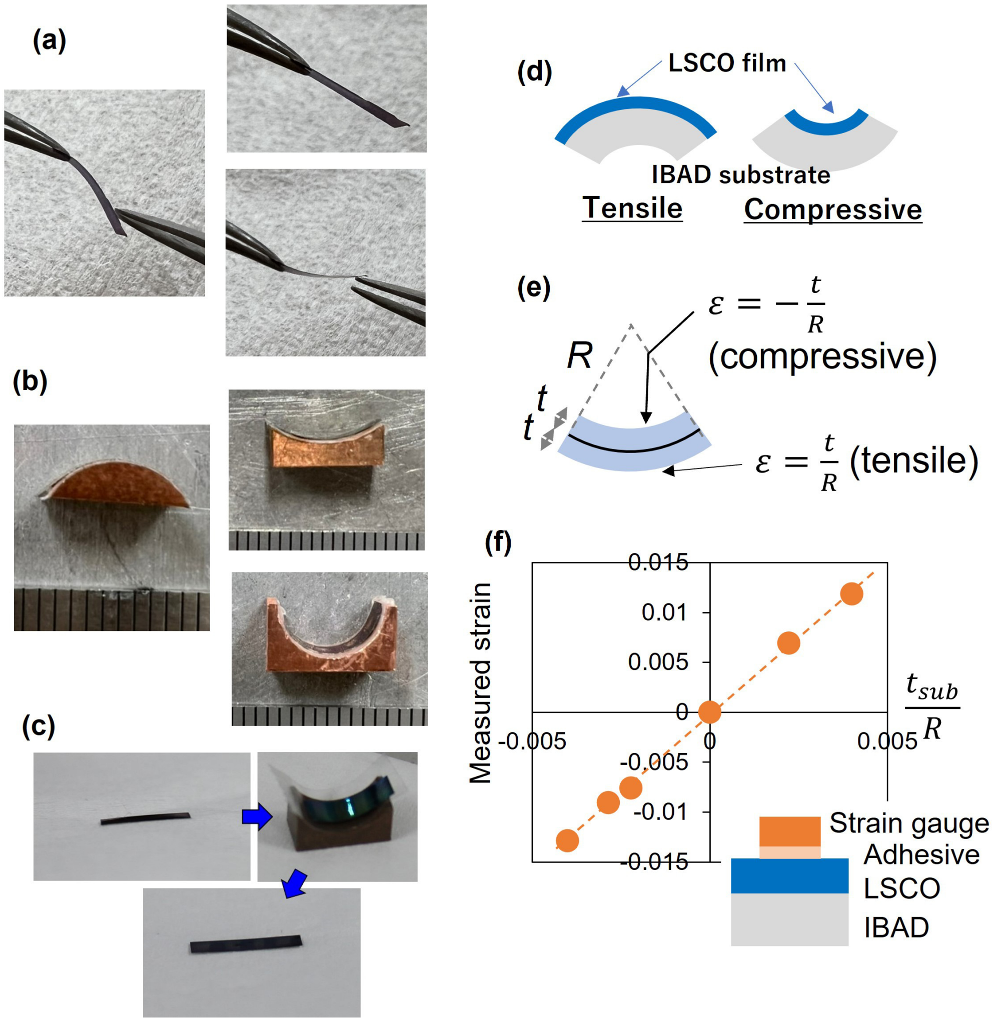

FIG. 2. Photographs of (a) the films bent by a tweezer and (b) the films placed on the Cu bending die. (c) The photographs of the films before bending and after bending (bending curvature = 5 mm). There is no residual strain in this photograph. (d) Schematic illustration of concave and convex bent films. (e) Strain values of each surface side of the bent films. (f) The surface strain measured by the strain gauge as a function of $t_{\text{substrate}}/R$ in the LSCO film under bending strain.

their maximally localized Wannier functions for this isolated band group.

III. RESULTS

A. Film bending and strain

The bending strain was applied to the LSCO films fabricated on an IBAD substrate. The IBAD substrate is usually used for $YBa_2Cu_3O_7$ coated conductors [35,36]. Figures 2(a) and 2(b) show photographs of the samples bent by a tweezer and on the Cu bending die. The single crystal substrate of oxides ($SrTiO_3$, $LaAlO_3$, etc.) cannot be deformed by a tweezer. The IBAD substrates with a large thickness are also difficult to bend. Thus, the substrates are usually difficult to deform by the small force that can be applied by hands or fingers. Figure 2(a) clearly shows the difference between the conventional films and the present films. Residual strain was not clearly observed after bending (bending curvature $\gtrsim$ 5 mm) in Fig. 2(c), indicating the elastic deformation at the small strain. At the bending radius of 4 mm, the plastic component was partially observed (returned to the slightly curved shape after removal from the die), but Fig. 2(c) indicates that the elastic component is dominant in the present range. The concave and convex sides in the bent tape result in compressive and tensile strain, which is schematically shown in Figs. 2(d) and 2(e). The tensile and compressive bending strains are given by $\frac{t_{\text{substrate}}}{R}$ and $-\frac{t_{\text{substrate}}}{R}$ in the single layer sample.

Figure 3 schematically shows the bending strain and stress for the multilayer sample consisting of the film and substrate. For simplicity, the bilayer structure is considered, but the multilayer structure of IBAD does not alter the conclusion that the Hastelloy dominates the bending situation (the neutral axis). The initial epitaxial strain and stress in the films are also schematically shown. By minimizing the energy of misfit dislocations and elastic strain, the epitaxial strain (elastic component), $\varepsilon_{\text{epitaxial}}$, is determined [23].

The stress is induced by the die to deform the shape from the unbent epitaxial film, and the total stress/strain consists of the epitaxial (initial) and bending stresses/strains. To discuss the T_c value, the total strain should be discussed because the total strain determines the lattice parameter. However, this

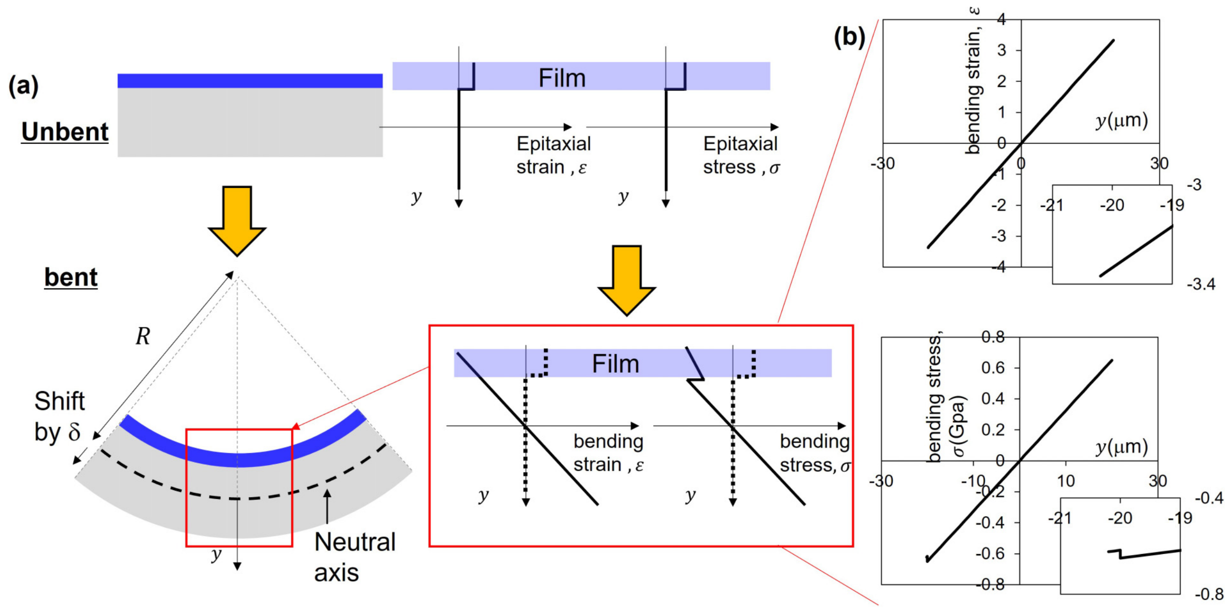

FIG. 3. (a) Schematic illustration of the bending/epitaxial strain and stress in the film. The film thickness is enlarged from the actual thickness for clarity. The total stress/strain (not shown) is the sum of the epitaxial stress/strain and bending stress/strain. (b) The dependence of the bending strain and stress on the position along the bending radius (y). $y < 20$ μm and -20 μm $< y < 20$ μm indicate the film and substrate positions, respectively. The stress and strain were calculated using the realistic values from the literature and assuming $\delta = 0$. Insets show the enlarged views near the film.

study focuses on the T_c variation from the unbent epitaxial film. The induced strain that causes the T_c variation is the bending strain, and the epitaxial strain exists regardless of the bending.

The neutral axis is in the center of the substrate in the case of the single layer, and the bending strain is given by $\pm\frac{t_{\text{substrate}}}{R}$ at the front/back of the substrate in the case of only the substrate. On the other hand, the neutral axis shift by δ should be considered when the film is deposited on the substrate. The bending strain varies linearly with the position along the direction of the bending radius. Due to the difference in Young's modulus between the film ($E_{\text{film}} = 185$ GPa [23]) and the substrate ($E_{\text{substrate}} = 195$ GPa [37]), the behavior of the bending stress is changed at the interface between the substrate and the film. The balance of the total stress determines the neutral axis. $\sigma(y)$ and $\varepsilon(y)$ are the total stress and strain depending on the position (y), respectively.

$$\begin{aligned}
\int_{-t_{\text{substrate}}-t_{\text{film}}}^{t_{\text{substrate}}} \sigma(y)dy &= \int_{-t_{\text{substrate}}}^{t_{\text{substrate}}} E_{\text{substrate}}\varepsilon(y)dy + \int_{-t_{\text{substrate}}-t_{\text{film}}}^{-t_{\text{substrate}}} E_{\text{film}}\varepsilon(y)dy \\
&= \int_{-t_{\text{substrate}}}^{t_{\text{substrate}}} E_{\text{substrate}}\frac{y-\delta}{R}dy + \int_{-t_{\text{substrate}}-t_{\text{film}}}^{-t_{\text{substrate}}} E_{\text{film}}\frac{y-\delta}{R}dy \\
&= -\frac{E_{\text{substrate}}}{R}\delta 2t_{\text{substrate}} - \frac{E_{\text{film}}}{2R}\left(2t_{\text{film}}t_{\text{substrate}} + t_{\text{film}}^2\right) - \frac{E_{\text{film}}}{R}\delta t_{\text{film}} \\
&= t_{\text{substrate}}\left(-\frac{2E_{\text{substrate}}}{R} - \frac{E_{\text{film}}}{R}\frac{t_{\text{film}}}{t_{\text{substrate}}}\right)\delta - \frac{E_{\text{film}}}{2R}\left(2 + \frac{t_{\text{film}}}{t_{\text{substrate}}}\right)t_{\text{film}} = 0. \qquad (1)
\end{aligned}$$

Here, the "epitaxial" component in the substrate and film is canceled in the integral. Because $\frac{t_{\text{film}}}{t_{\text{substrate}}} \ll 1$ ($t_{\text{film}} < 190$ nm and $2t_{\text{substrate}} = 40$ μm) and $E_{\text{film}} \sim E_{\text{substrate}}$,

$$t_{\text{substrate}}\left(-\frac{2E_{\text{substrate}}}{R}\delta - \frac{E_{\text{film}}}{R}t_{\text{film}}\right) = 0, \qquad (2)$$

$\delta = -\frac{E_{\text{film}}}{2E_{\text{substrate}}}t_{\text{film}}$. Considering the modified neutral axis, the bending strains at the film bottom and surface are

$$\frac{-t_{\text{substrate}} - \delta}{R} = \frac{-t_{\text{substrate}}}{R}\left(1 - \frac{E_{\text{film}}}{2E_{\text{substrate}}}\frac{t_{\text{film}}}{t_{\text{substrate}}}\right) \sim \frac{-t_{\text{substrate}}}{R}, \qquad (3a)$$

$$\frac{-t_{\text{substrate}} - t_{\text{film}} - \delta}{R} = \frac{-t_{\text{substrate}}}{R}\left(1 + \frac{t_{\text{film}}}{t_{\text{substrate}}} - \frac{E_{\text{film}}}{2E_{\text{substrate}}}\frac{t_{\text{film}}}{t_{\text{substrate}}}\right) \sim \frac{-t_{\text{substrate}}}{R}. \qquad (3b)$$

Because the film thickness is very thin compared with the substrate thickness (<1%), the influence of the film thickness on the neutral axis and the bending strain can be neglected. Thus, the strain in the film can be assumed to be constant throughout the film.

Here, we roughly calculate the bending strain values for the film bottom and surface to confirm the above conclusion on the film strain. $t_{\text{substrate}}$ is 20 μm for the film bottom and 20 μm+200 nm for the film surface. The total strain is 0.003 33 at the bottom and 0.003 37 at the top. The strain difference is only 0.000 04, which is much smaller than the strain range discussed in this study. Thus, the strain difference in the film along the thickness is negligible.

To confirm the successful control of the bending strain, the strain of the film surface was measured using a strain gauge. Figure 2(f) shows the strain measured by the strain gauge as a function of $t_{\text{substrate}}/R$, where $2t_{\text{substrate}}$ is the substrate thickness and R is the bending curvature. The substrate thickness ($2t_{\text{substrate}} = 40$ μm) dominates the sample thickness because the film thickness ($t_{\text{film}} < 200$ nm) is very thin as already discussed.

The strain gauge cannot give the accurate strain at the surface (~film) because the adhesive and strain gauge have a thickness comparable to the sample. Assuming that the bending strain at the surface of the sample is given by $t_{\text{substrate}}/R$, the strain measured by the strain gauge is larger than this value. Figure 2(f) shows the strain gauge value as a function of $t_{\text{substrate}}/R$. As shown in Supplelmental Material Fig. S3 [32], the strain gauge value can be explained by considering the adhesive+gauge thickness. The difference between $t_{\text{substrate}}/R$ and the measured strain is explained by considering the adhesive+gauge thickness of 30 μm. Thus, the validity of the surface strain given by $t_{\text{substrate}}/R$ is demonstrated by the linear relationship for the strain gauge measurement by considering the adhesive and gauge thickness.

The strain is applied to the films as the elastic strain, dislocation, and crack. It should be noted that the relaxation of the film strain by dislocations requires the dislocation motion [38]. In the metal films where the dislocation can move [39] or the oxide films deposited at high temperature, the strain is relaxed by the dislocation after the threading dislocations and/or the surface dislocation loops move to spread the misfit dislocations along the interface. It is well known that plastic deformation is difficult in ceramics such as oxides because the dislocation motion is difficult. Therefore, it is assumed that configurational variation of the misfit dislocations does not occur at the interface in the case of room temperature bending. If the dislocation configuration at the interface is unchanged, the strain relaxation by the dislocations does not occur. It has been reported that the elastic component is relaxed by dislocations only at the high temperature in the bending of GaAs/$\text{In}_x\text{Ga}_{1-x}\text{As}$/GaAs [40]. Thus, the strain relaxation by dislocations is not dominant in this case.

Crack formation increases resistivity because it degrades the current flow path. However, the significant resistivity increase was not observed in the compression cases. In addition, the crack irreversibly changes the properties. As shown later, the property exhibits reversible behavior. These suggest that the crack formation is not a dominant component of the strain.

Thus, the dislocations and fracture (crack) are excluded from the dominant component of the strain. It has been reported that the ratio of the lattice strain and applied strain is 0.57 for YBCO and 0.88 for Hastelloy and the YBCO coated conductors [41]. The transferred strain for YBCO is 64% of the strain in the substrate. YBCO has two types of domains (orthorhombic structure with different a-axis and b-axis lengths), resulting in stress concentration. On the other hand, LSCO has no domain structure (tetragonal structure with $a = b$). This suggests that the present LSCO situation is further away from YBCO in terms of the stress concentration. It is reasonable to assume that the bending strain is applied to the LSCO films mainly as the elastic strain. This is also consistent with the observation in Fig. 2(c) that the curved film was returned elastically to the straight film after the bending strain is removed.

B. T_c variation induced by strain

Figures S4–S6 [32] show the XRD results for the films, indicating the epitaxial films on the IBAD substrate. The lattice parameter is slightly larger than that in the bulk LSCO [42] in Fig. S7(a) [32]. Figures 4 and S8 [32] show the ρ-T curve for various Sr contents and thicknesses which vary the electronic structure and T_c. The resistivity decreases with increasing the Sr content due to the hole doping (Fig. S5 [32]). The resistivity for $x = 0.15$ is ~1000 μΩ cm. The resistivity is of the same order but may be slightly higher than the bulk LSCO [42]. The optimum T_c for bulk LSCO is 40 K, but the T_c in this study is lower. As shown in Fig. S7(b) [32], the T_c-c relationship is different between the film and the bulk [42], indicating that the carrier or band structure in the present films is not the same as that in the bulk. The lattice parameter and resistivity values may indicate that the oxygen vacancies or the lattice defects near the substrate reduce the T_c.

Figures 4 and S8 [32] show the ρ-T curve as a function of the strain. In the case of $x = 0.15$, the compressive strain of -0.005 (bending curvature = 4 mm) increased the T_c from 23.4 K (unbent) to 27.3 K. On the other hand, the tensile strain of 0.004 (bending curvature = 5 mm) decreased the T_c from 23.4 K (unbent) to 19.1 K. In the case of $x = 0.1$ and 0.2, similar T_c variation by the bending strain was observed (not shown for the tensile case of $x = 0.1$ and the case of $x = 0.2$).

The thickness varied the superconductivity in the unbent films due to the epitaxial strain (Fig. S6 [32]), but the T_c variation by the bending strain was observed regardless of thickness in Fig. 4(e). In the case of $x = 0.25$, while the superconductivity was not observed in the unbent film, superconductivity starts to appear under the compressive strain of -0.0022. Figure 4(f) shows the ρ-T curves for the unbent and bent LSCO films with $x = 0.1$, whose preparation condition is different from that in Fig. 4(c) due to the change of chamber setup. In Fig. 4(f), the bending was performed by placing the film in the U-shaped die which is shown in the inset of Fig. 4(f). It should be noted that the superconducting transition is induced by the compressive bending in Fig. 4(f). The observations in Fig. 4 demonstrate that the superconductivity in the LSCO flexible films can be controlled by the external bending strain.

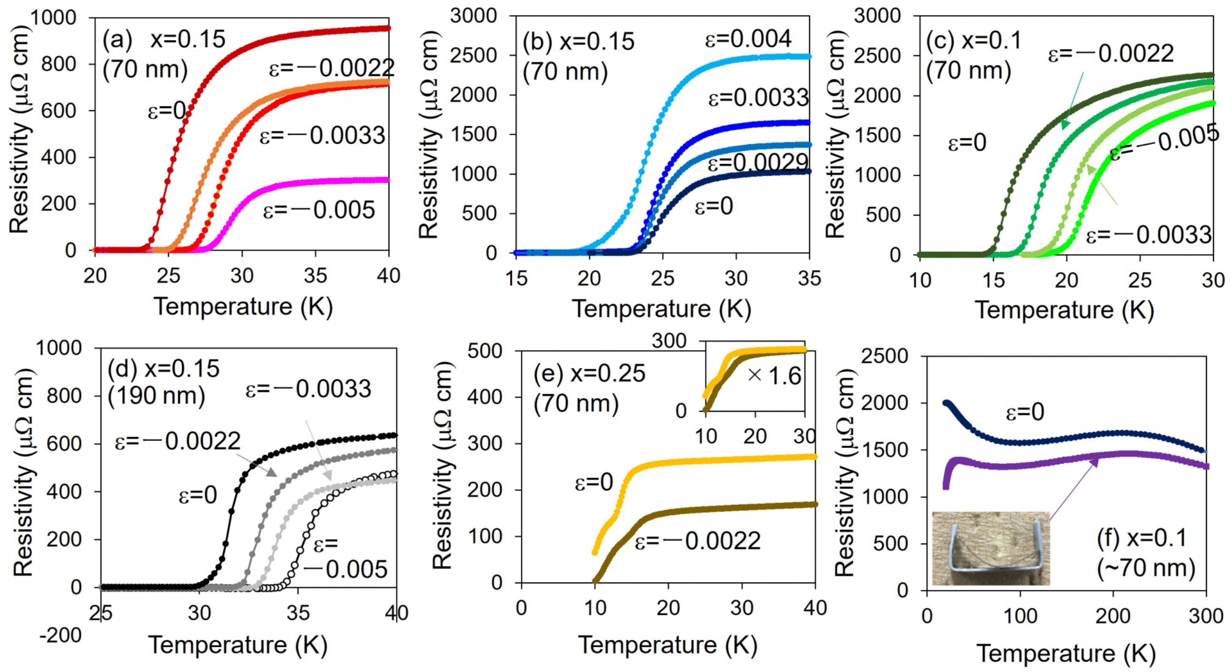

FIG. 4. Temperature dependence of resistivity (ρ) for (a) the compressive-bent LSCO(0.15), (b) the tensile-bent LSCO(0.15), (c) the compressive-bent LSCO(0.1), (d) the compressive-bent thick LSCO(0.15), (e) the compressive-bent LSCO(0.25), and (f) the compressive-bent thick LSCO(0.1). Inset of (f) shows the sample setup for bending.

Figure 5 shows the ρ-T curves in magnetic fields of 0, 1, 3, 5, 7, and 9 T for $\varepsilon = 0$ and $\varepsilon = -0.004$ (bending radius = 5 mm). As in Fig. 4, the compressive strain of -0.004 increased the T_c from 22.7 K(unbent) to 26.2 K. Regardless of magnetic field, the resistance drop was shifted to high temperature by the compressive strain. Thus, the bending strain increases the irreversibility temperature (T_{irr}) in magnetic field, as well as the T_c. The T_{irr} nearly corresponds to the phase boundary between the glass and liquid phases of vortices although it is not a strict physical definition [43,44]. Figure 5(b) shows the T_{irr}-B curves for $\varepsilon = 0$ ($x = 0.15$), $\varepsilon = -0.004$ ($x = 0.15$) which are compared with that for the $\varepsilon = 0$ ($x = 0.2$). With the increase in the Sr content, x improved the T_{irr}-B curve to the high temperature side as shown in Fig. 5(b). The Sr content affects the vortex pinning. On the other hand, the compressive strain also improved the curve, although the structural factor such as the Sr content was not varied. Figure 5(b) indicates the variation in $B_{irr}(0)$. The pinning center structure is not changed by the compressive strain, and the variation in the pinning energy should be discussed [45]. The pinning energy is determined by the coherence length and the penetration depth. The coherence length is determined by the gap energy and the Fermi velocity [46]. The relationship between the coherence length and the penetration depth, and the electronic structure in high-T_c superconductors with the nodal gap [47] should be clarified. It has been reported that the normal state carrier concentration measured by the Hall effect decreases with overdoping in LSCO [48]. The relationship between the normal state carrier concentration and the superfluid density is still unclear because Fermi surface reconstruction may occur [49]. The detailed electronic structure calculation in the next section may help in discussing this matter. However, Fig. 5 demonstrates that the strain can control the vortex phase diagram through the pinning energy. The present observation seems to be consistent with the report that the overdoping improves the J_c in the YBCO film [50]. Thus, the control of the pinning energy and J_c by strain is an interesting topic which includes the influence of the strain not only on the T_c, but also on the superfluid density, the coherence length, and the penetration depth.

Figure 6 shows the T_c variation with the bending history (no strain and compressive strain) for the LSCO (0.15, 90 nm). The T_c variation for the bending history of no strain, tensile strain, and compressive strain is also shown in Fig. S9 [32]. After placing the sample on the die, gold wires were attached using silver paste. The T_c measurement (in the temperature from 300 to 10 K) was performed. After increasing the temperature, the sample was removed from the measurement apparatus. The sample was detached from the sample die, and the sample was placed on the next die. After that, the T_c measurement was measured again from 300 to 10 K. When the sample contained the slight plastic component (4 mm bending), the straight shape was maintained by placing the sample on the straight holder with a doublesided tape. The strain history is shown in Fig. 6(a). The strain of -0.002 to -0.005 was applied to measure the T_c, and the T_c was also measured at the unbent situation. Figure 6(b) shows the T_c variation for the bending history of Fig. 6(a). The T_c value returned to that of the unbent film after the bending, indicating the reversible response of superconductivity to the bending strain. The resistivity decreased significantly in cases 3 and 8 maybe due to an unintended current path to the metal substrate.

The T_c variation in the present study is ~5 K, while the epitaxial [51–53] and nanocomposite [54] strains for LSCO increased T_c to ~50 K. The strain configuration is different from that in the epitaxial and nanocomposite strains. The

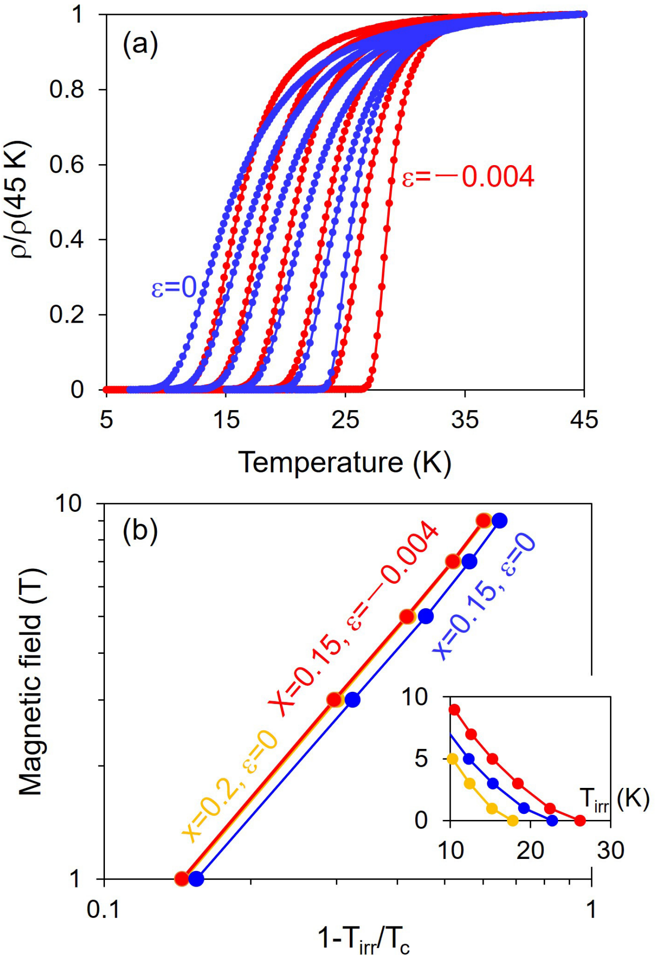

FIG. 5. (a) ρ/ρ (45 K)-T curves in the magnetic field of 0, 1, 3, 5, 7, and 9 T for the LSCO(0.15, 70 nm) with $\varepsilon = 0$ and $\varepsilon = -0.004$. (b) B-$(1 - T_{\text{irr}}/T_c)$ curves for the LSCO (0.15, 70 nm) of $\varepsilon = 0$ and $\varepsilon = -0.004$. For comparison, the B-$(1 - T_{\text{irr}}/T_c)$ curve for the LSCO (0.2) with $\varepsilon = 0$.

important observation in the experimental part is that the T_c was varied by the variable external strain (Fig. 4) and the reversible strain (Fig. 6) in a single film. The sign and magnitude of the strain cannot be varied after finishing the sample preparation in usual systems including the epitaxial films. From the reversibility point of view, the T_c variation induced by external strain is very different from the situation for the epitaxial strain.

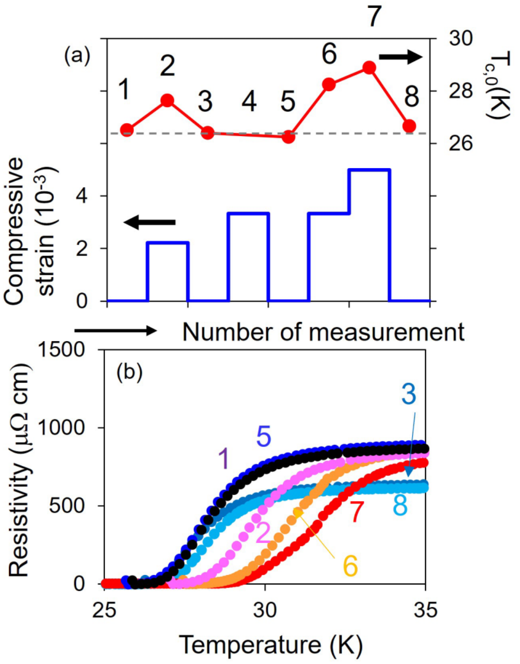

FIG. 6. (a) Bending history and T_c variation for the repeated bending for the LSCO (0.15, 90 nm). (b) ρ-T curves for the bending history shown in (a).

C. Apex oxygen effect

The crystalline anisotropy and the Poisson effect affect the lattice and atomic configuration under the bending. Here, the atomic and electronic structures are analyzed in detail to understand the influence of the bending strain on T_c. In this section, we investigate the mechanism of the T_c variation induced by external strain. For this purpose, we perform *ab initio* density functional calculation and Wannier function analysis. We first perform the analysis for Wannier orbital energies. For this purpose, we define oxygens in the CuO_6 with the numbers 1–4 in Fig. 7(a). In cuprates, it is known that there is a close correlation between the T_c and the octahedral oxygen energy level [55]. Then, we consider several characteristic energies; the energy level of the apex oxygen O(A) [O1 and O2 atoms in Fig. 7(a)] relative to the in-plane oxygen O(P) (O3 and O4 atoms) as

$$\Delta v_A = v_{O(A)} - v_{O(P)} \tag{4}$$

with

$$v_{O(A)} = \frac{1}{6} \sum_{\alpha=x,y,z} \left(E_{\text{O1-}p_\alpha} + E_{\text{O2-}p_\alpha}\right) \tag{5}$$

and

$$v_{O(P)} = \frac{1}{6} \sum_{\alpha=x,y,z} \left(E_{\text{O3-}p_\alpha} + E_{\text{O4-}p_\alpha}\right), \tag{6}$$

where E_μ is the μth Wannier orbital energy, all of which are listed in Supplemental Material Table S1 [32]. We also consider the energy level of the in-plane oxygen O(P) relative to the in-plane copper Cu(P) in Fig. 7(a) as

$$\Delta v_M = v_{O(P)} - v_{Cu(P)} \tag{7}$$

with

$$v_{Cu(P)} = \frac{1}{5} \sum_{\alpha}^{5} E_{\text{Cu-}d_\alpha} \tag{8}$$

and $\alpha = xy,\ yz,\ zx,\ z^2$, and $x^2 - y^2$. Finally, we consider Δv_d as an energy difference between the Cu-d_{z^2} and Cu-$d_{x^2-y^2}$ orbitals as

$$\Delta v_d = \sqrt{\left(E_{\text{Cu-}d_{z^2}} - E_{\text{Cu-}d_{x^2-y^2}}\right) + 4\Delta_{z^2,\,x^2-y^2}} \tag{9}$$

with $\Delta_{z^2,\,x^2-y^2}$ being the on-site transfer between the Cu-d_{z^2} and Cu-$d_{x^2-y^2}$ orbitals.

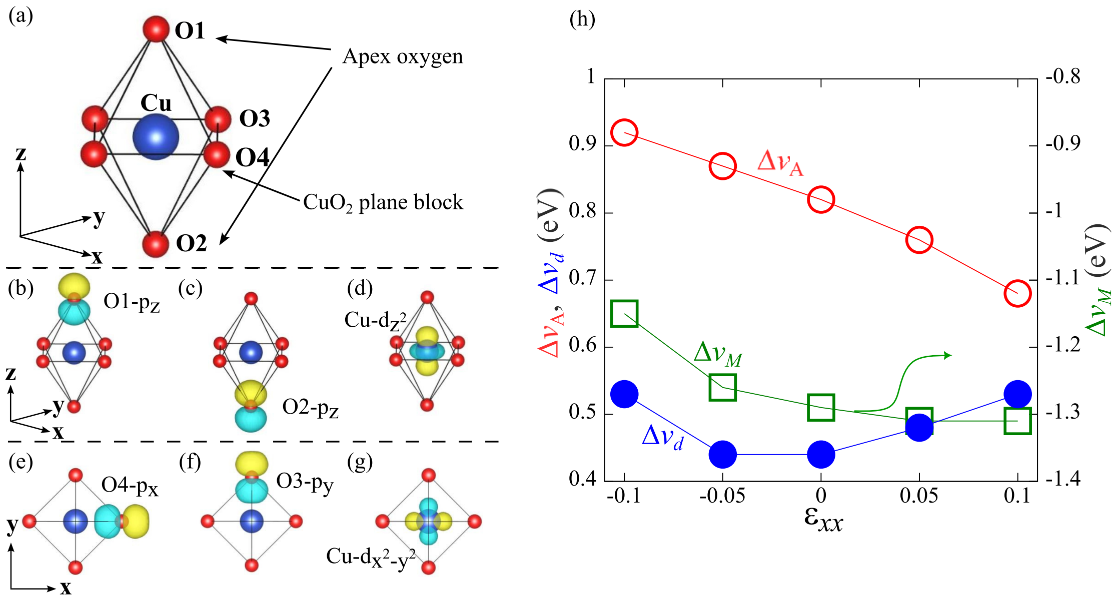

FIG. 7. (a) A schematic figure of a CuO_6 octahedron consisting of O1–O4 and Cu atoms. We show visualization of important Wannier orbitals (drawn by VESTA [56]): The panels (b) and (c) are p_z orbitals of the apex oxygen, and (e) and (f) display the p_x and p_y orbitals in the CuO_2 plane, respectively. We also show (d) Cu-d_{z^2} and (g) Cu-$d_{x^2-y^2}$ orbitals. (h) Strain dependence of orbital energies, where Δv_A in Eq. (4) (circles) is the energy level of the apex oxygen relative to the in-plane oxygen, Δv_M in Eq. (7) (squares) is the energy level of the in-plane oxygen relative to the in-plane Cu, and Δv_d in Eq. (9) (bullets) is the difference between the d_{z^2} and $d_{x^2-y^2}$ of Cu.

We show in Fig. 7(h) the strain dependence of Δv_A, Δv_M, and Δv_d, whose quantitative values are summarized in Table S1 [32]. From the figure, we see that the Δv_A decreases from compressive to tensile configurations; $\frac{d\Delta v_A}{d\varepsilon} < 0$. Also, from Fig. 4, the T_c decreases from compressive to tensile configurations; $\frac{dT_c}{d\varepsilon} < 0$. Thus, $(dT_c/d\varepsilon)/(d\Delta v_A/d\varepsilon) \sim \frac{dT_c}{dv_A} > 0$; the T_c increases with Δv_A, which is consistent with the observation of Ref. [55]. The Δv_M also decreases with strain ε, but the tendency is weak. Also, the Δv_d exhibits a quadratic feature to the ε. It should be noted here that the height of the apex O(A) oxygen from the CuO_2 plane is larger in the compressive structure with introducing the Poisson's ratio (see Fig. 1). Then, our observed Δv_A trend simply might reflect the height difference.

D. Two-orbital analysis

We next perform an analysis for the strain dependence, focusing on two orbitals in the cuprate. The two-orbital model considering the $d_{x^2-y^2}$ [Fig. 7(g)] and d_{z^2} [Fig. 7(d)] orbitals has been used for discussions of the superconducting tendency of cuprates [57]. For example, the T_c difference between $La_{2-x}Sr_xCuO_4$ ($T_c \sim 40$ K) and $HgBa_2CuO_{4+\delta}$ ($T_c \sim 90$ K) can be explained from the difference in the weight of the d_{z^2} orbital to the Fermi surface; in the latter higher-T_c Hg compound, the d_{z^2} weight is smaller and dominated by the single-orbital nature of the $d_{x^2-y^2}$ orbital. This picture may be useful in the present discussion about the bending-strain effect in $La_{2-x}Sr_xCuO_4$ on T_c; in the experiment, the compressive strain leads to the T_c increase, while the tensile strain brings about the T_c decrease.

We show in Fig. 8 a fat-band plot for the band structure near the Fermi level. From top to bottom, the fat-band plots for the strain $\varepsilon_{xx} = -0.1,\ -0.05,\ 0,\ 0.05$, and 0.1 are shown. The left panels display schematic figures for strained structures. The second left panels are results on the Cu-d_{z^2} contribution denoted by green to the band structure, and the second right panels show results on the Cu-$d_{x^2-y^2}$ contribution denoted by blue. We also give in the right panels contributions from these two orbitals to the density of states (DOS). We see that the low-energy electronic structure near the Fermi level is mainly contributed from the Cu-$d_{x^2-y^2}$ orbital, while the Cu-d_{z^2} contribution gradually increases from the compressive- to tensile-bent structure.

TABLE I. Comparison of local density of states (DOS) of each orbital at the Fermi level, where ρ_{z^2}, $\rho_{x^2-y^2}$, $\rho_{O(A)}$, and $\rho_{O(P)}$ are local DOS of Cu-d_{z^2}, Cu-$d_{x^2-y^2}$, apex oxygen, and in-plane oxygen, respectively, and ρ_{total} is the total DOS at the Fermi level. The unit is given in states/eV. We also list the ratios of $\rho_{z^2} + \rho_{O(A)}$ and $\rho_{x^2-y^2} + \rho_{O(P)}$ to ρ_{total}.

ε_{xx}	-0.1	-0.05	0	0.05	0.1
ρ_{z^2}	0.03	0.04	0.08	0.20	0.31
$\rho_{x^2-y^2}$	0.34	0.37	0.42	0.51	0.53
$\rho_{O(A)}$	0.04	0.05	0.08	0.19	0.29
$\rho_{O(P)}$	0.36	0.37	0.41	0.53	0.58
ρ_{total}	0.78	0.84	1.00	1.43	1.71
$\frac{\rho_{z^2}+\rho_{O(A)}}{\rho_{\text{total}}}$	0.09	0.11	0.16	0.27	0.35
$\frac{\rho_{x^2-y^2}+\rho_{O(P)}}{\rho_{\text{total}}}$	0.90	0.88	0.83	0.73	0.65

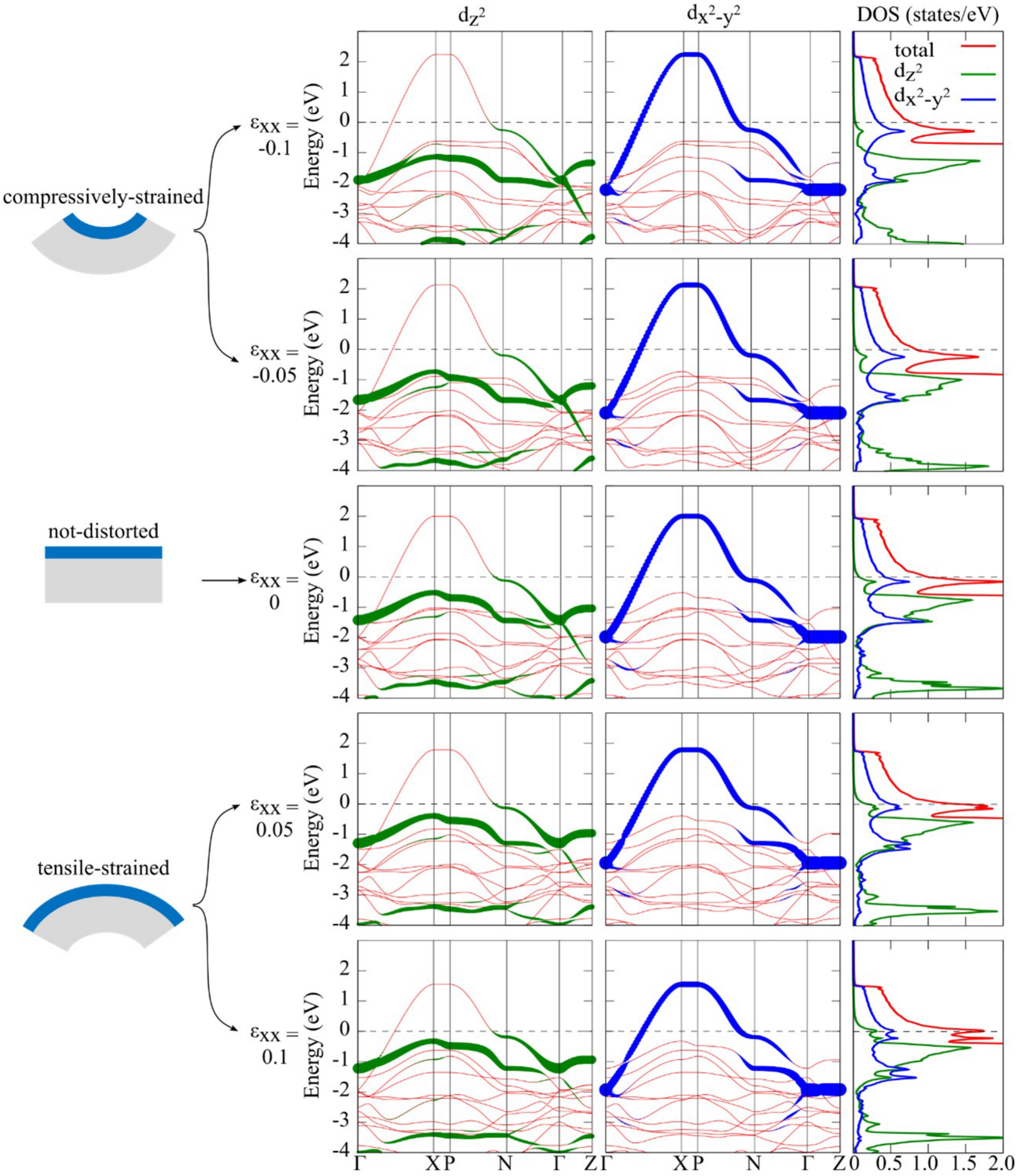

FIG. 8. Fat-band plots: From top to bottom, the fat bands for strain $\varepsilon_{xx} = -0.1,\ -0.05,\ 0,\ 0.05$, and 0.1 are shown. The left panels display schematic figures of strained samples. The second left panels are the results on the Cu-d_{z^2} contribution denoted by green, and the second right panels show the results on the Cu-$d_{x^2-y^2}$ contribution denoted by blue. The contributions to the density of states from these orbitals are shown in the right panels.

To show this trend quantitatively, we summarized in Table I the local DOS of each orbital at the Fermi level. In this table, we add the DOS contributions from the apex oxygen O(A) and the in-plane oxygen O(P), as well as the Cu-d_{z^2} and Cu-$d_{x^2-y^2}$ contributions. The total DOS ρ_{total} at the Fermi level is basically given as $\rho_{z^2} + \rho_{x^2-y^2} + \rho_{\mathrm{O}(A)} + \rho_{\mathrm{O}(P)}$. It should be noted here that, in the cuprate, the $d_{x^2-y^2}$ orbital is well hybridized with neighboring in-plane O3-p_y [Fig. 7(f)] and O4-p_x [Fig. 7(e)] orbitals, and the d_{z^2} orbital is hybridized with apex O1-p_z [Fig. 7(b)] and O2-p_z [Fig. 7(c)] orbitals.

We summarized in Fig. 9 the dependence of $(\rho_{x^2-y^2} + \rho_{\mathrm{O}(P)})/\rho_{\text{total}}$ and $(\rho_{z^2} + \rho_{\mathrm{O}(A)})/\rho_{\text{total}}$ on the bending strain ε_{xx}. We see that the compressive-bent structure $(\varepsilon_{xx} < 0)$ gives a large $(\rho_{x^2-y^2} + \rho_{\mathrm{O}(P)})/\rho_{\text{total}}$, while the tensile-bent structure $(\varepsilon_{xx} > 0)$ leads to a small $(\rho_{x^2-y^2} + \rho_{\mathrm{O}(P)})/\rho_{\text{total}}$. In the experiment, the compressive-bent structure gives a higher T_c, while the tensile-bent structure leads to a smaller T_c. Thus, the higher T_c structure corresponds to the compressive-bent structure giving the large $(\rho_{x^2-y^2} + \rho_{\mathrm{O}(P)})/\rho_{\text{total}}$ and small $(\rho_{z^2} + \rho_{\mathrm{O}(A)})/\rho_{\text{total}}$.

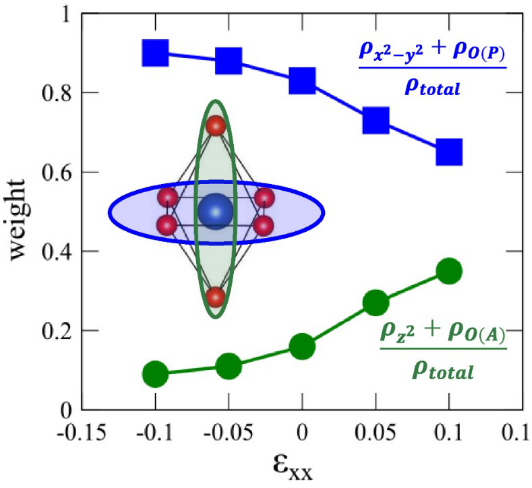

FIG. 9. Calculated dependence of $(\rho_{x^2-y^2}+\rho_{O(P)})/\rho_{\mathrm{total}}$ and $(\rho_{z^2}+\rho_{O(A)})/\rho_{\mathrm{total}}$ on the bending strain ε_{xx}.

This is consistent with the view of Ref. [57]. We note that the ρ_{total} itself also becomes large from the compressive- to tensile-bent structure (0.78→1.72).

IV. DISCUSSION

A. Influence of doping and thickness on T_c variation

Figure 10 shows the strain dependence of ΔT_c in the films discussed in Fig. 4, where ΔT_c is given by T_c(bent) − T_c(unbent). The ΔT_c decreases with increasing the strain. The ΔT_c-strain relationship does not depend on the carrier concentration and the epitaxial strain (thickness). The T_c variation by the compressive strain is larger than that by the tensile strain. The inset of Fig. 10(c) compares the ΔT_c-strain relationship in the present bent films and epitaxial films [18]. It is assumed that the epitaxial strain is equal to the lattice mismatch between the film and substrate. The T_c variation by the epitaxial strain is larger than that by the bending strain. While the epitaxial strain is applied along the two in-plane directions, the bending strain is applied only along the longitudinal direction. As a result, the strain dependence was more significant for the epitaxial films than in the bending case.

The DFT calculations for the parent material La_2CuO_4 suggest that the bending strain can affect details of the low-energy electronic structure, and especially, the balance of orbital occupancies in and perpendicular to the CuO_2 plane. In the experiments for LSCO, as shown in Fig. 10, the T_c-strain slope is unchanged with the doping concentration and film thickness (initial epitaxial strain). Thus, we think that the T_c dependence on strain is basically determined by the

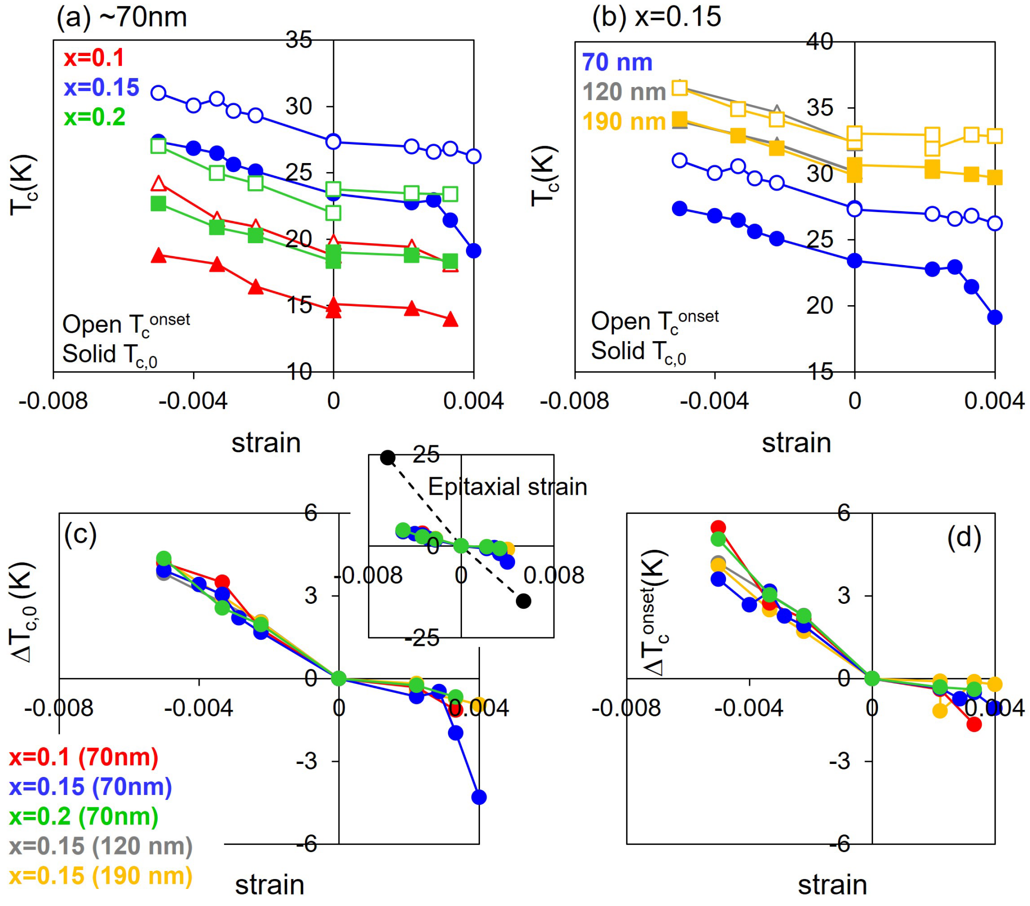

FIG. 10. T_c as a function of strain for (a) $x = 0.1$–0.2 and (b) thickness of 70–190 nm. A strain dependence of (c) $\Delta T_{c,0}$ and (d) $\Delta T_c^{\mathrm{onset}}$ for $x = 0.1$–0.2 and thickness of 70–190 nm. The same symbols are used for (c) and (d) to show the same sample. Inset of (c) compares the strain dependence of ΔT_c for the bending and the epitaxial [18] strains.

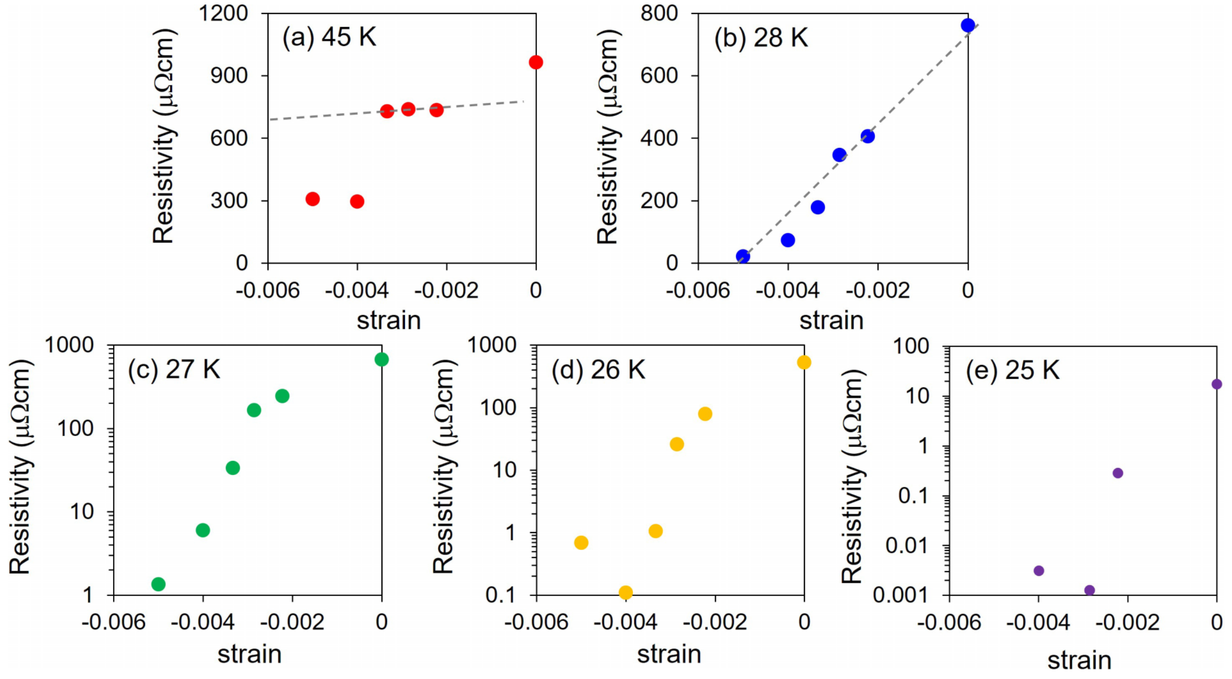

FIG. 11. Resistivity as a function of strain for the LSCO(0.15, 70 nm) at the temperatures of (a) 45 K, (b) 28 K, (c) 27 K, (d) 26 K, and (e) 25 K. (c), (d), and (e) are a logarithmic plot for resistivity. The dashed lines are the fitting line to obtain $\Delta R/\Delta\varepsilon$.

electronic-structure details such as orbital occupations rather than the doping situation and thickness.

B. Possible application

The T_c variation induced by external strain is a very interesting fundamental phenomenon. This phenomenon may be available for application. As shown in Fig. 2(a), a small tweezer force can be very sensitively detected by the T_c change in the present films. To compare the resistivity variation with metals and semiconductors which are the conventional strain sensor materials, the gauge factor is discussed [5]. Figure 11 shows the resistivity as a function of strain at the temperatures of 45 and 28–25 K (near T_c). The gauge factor is given by $(\Delta R/R)/\Delta\varepsilon$, where ΔR and $\Delta\varepsilon$ are the resistivity and strain variations, respectively [5]. $(\Delta R/R_0)/\Delta\varepsilon = \{R(\varepsilon_0 + \Delta\varepsilon) - R_0\}/(R_0\Delta\varepsilon)$, where $R_0 = R(\varepsilon_0)$ is the resistance at the strain reference, ε_0. According to the present result, while resistivity $=$ (normal state resistivity) at $\varepsilon = 0$ near T_c^{onset}, resistivity $= 0$ at the finite strain which can realize the superconductivity due to the strain-induced T_c increase. $\varepsilon = -0.005$ increased the T_c by $\sim$5 K in the present LSCO films whose transition width, ΔT_c, is approximately a few kelvin. In this case, when the gauge factor is determined by the normal state resistivity as the strain reference ($R_0 =$ normal state resistivity), the gauge factor is roughly estimated to be $\sim(0 - R_0)/R_0\varepsilon = 1/0.005 = 200$, which is as large as that for the semiconductors. The LSCO films as a strain sensor have more of an advantage due to the coexisting nature of the low resistivity than semiconductors and the large gauge factor.

If we set the reference strain to the superconducting state ($R_0 = 0$), the gauge factor is ∞. The selection of the strain reference, namely, the R_0, significantly affects the gauge factor because the resistivity variation with the strain is very large (several orders of magnitude). As for $\Delta R/\Delta\varepsilon$, the linear fitting should be avoided in the wide range because of the nonlinearity near T_c as shown in Fig. 11, and the linear fitting is performed for the narrow strain range. On the other hand, the linear fitting is possible at the temperature of 28 K as shown in Fig. 11(b). The same definition of gauge factor should be used to compare the strain sensitivity of LSCO with metals and semiconductors. Considering these points, the procedure to obtain the gauge factor in Table II is as follows: After confirming the reasonable dependence of resistivity on strain in Fig. 11, $\Delta R/\Delta\varepsilon$ was obtained using the two adjacent data points for 25–27 K and the linear fitting in Fig. 11 for 28 and 45 K. The normalization by R_0 was performed for $\Delta R/\Delta\varepsilon$ at the strain references near the superconducting ($R_0 \sim 0$) state and at the normal state. The results are shown in Table II. Here, the comparison of the gauge factors determined at the different strain reference is meaningful to select the strain range for the sensor application with the initial strain offset. The sensitivity (gauge factor) near T_c is two to five orders

TABLE II. Gauge factor for metal, semiconductor, and the present LSCO/IBAD (0.15, 70 nm). For the LSCO, different strain references denoted by ε_0 are used.

	Gauge factor
Metal	2–4 [5]
Semiconductor	30–170 [5]
LSCO/IBAD (45 K)	$8.6(\varepsilon_0 = -0.0022)$, $8.7(\varepsilon_0 = -0.0033)$
LSCO/IBAD (28 K)	$210(\varepsilon_0 = 0)$, $7300(\varepsilon_0 = -0.005)$
LSCO/IBAD (27 K)	$1200(\varepsilon_0 = -0.0033)$, $3400(\varepsilon_0 = -0.005)$
LSCO/IBAD (26 K)	$1100(\varepsilon_0 = -0.0022)$, $50\,000(\varepsilon_0 = -0.0033)$
LSCO/IBAD (25 K)	$1600(\varepsilon_0 = -0.0022)$, $350\,000(\varepsilon_0 = -0.0029)$

higher than the conventional materials especially when we choose the superconducting state as the strain reference. To take advantage of this high sensitivity, the reference state should be appropriately selected and implemented in the device (e.g., give the initial strain offset at the reference state).

Liquid hydrogen with a boiling temperature of 20 K is important for the future hydrogen society, where the mechanical destruction of liquid hydrogen containers should be avoided for safety reasons. Fusion requires a high magnetic field of 20 T, which is generated by a superconducting magnet operating at 20 K. The superconducting coil is accidentally damaged by the electromagnetic force. Detecting the mechanical damage at an early stage makes the operation of the magnet controllable, safe, and stable. Therefore, a sensitive strain sensor is required to detect the mechanical damage at the earlier stage. The resistivity variation near T_c realizes the sensitivity two to five orders higher than the semiconductors and metals. Although the superconducting strain sensor is only available at low temperatures, it is very promising for managing the mechanical stability of cryogenic equipment such as liquid hydrogen containers and superconducting coils.

V. SUMMARY

The LSCO films were fabricated on the IBAD substrates and bent in the die to observe the T_c and resistivity variation by external strain. The compressive bending strain of -0.005 increased the T_c from 23.4 K (unbent) to 27.3 K. This T_c variation is larger than that previously reported in YBCO, which is consistent with the fact that LSCO is markedly sensitive to the strain. The irreversibility temperature was improved by the compressive strain due to the change in the pinning energy. Furthermore, the reversible strain changed the T_c depending on the magnitude of the strain, suggesting the response of superconductivity in the flexible LSCO films to the variable external strain for sensor device application. To understand the observed experimental results, *ab initio* density-functional calculation for the mother compound La_2CuO_4 was performed. We found that the low-energy electronic structure is sensitive to the bending strain; a compressive strain with considering Poisson's ratio causes the apex oxygen to move away from the CuO_2 plane, and conversely, a tensile strain brings it closer. This greatly changes the balance between the perpendicular orbital group to the CuO_2 plane and the in-plane orbital group in the density of states in the Fermi level. We found that, by changing from the compressive strain to the tensile strain, the contribution of the perpendicular orbital group becomes larger, and the contribution of the in-plane orbital group becomes smaller. This indicates that under the compressive strain, carriers (holes) are preferentially injected into the in-plane orbitals, while under the tensile strain, this preference is inhibited. Thus, the compressive strain in LSCO is favorable for higher T_c, being consistent with the experimental observations. The T_c and resistivity in the cuprate superconductor under reversible external strain is a new aspect of the superconducting cuprates, which opens the monitoring of the mechanical situation for the stable operation of cryogenic systems without unintended fatigue.

ACKNOWLEDGMENTS

This work was supported by JSPS, Grant-in-Aid for scientific research Grants No. 22K18812, No. 22H01183, and No. 23H01126. The IBAD substrates were supplied by Faraday Factory Japan.

---

[1] V. Vashishtha and L. T. Clark, Microelectron. J. **107**, 104942 (2021).

[2] J. G. Zhu and C. Park, Mater. Today **9**, 36 (2006).

[3] A. Georgopoulou, S. Michel, B. Vanderborght, and F. Clemens, Sens. Actuators A **318**, 112433 (2021).

[4] J. Li, L. Fang, B. Sun, X. Li, and S. H. Kang, J. Electrochem. Soc. **167**, 037561 (2020).

[5] A. S. Fiorillo, C. D. Critello, and S. A. Pullano, Sens. Actuators A **281**, 156 (2018).

[6] T. Aoyama and K. Ohgushi, Phys. Rev. Mater. **8**, L041402 (2024).

[7] M. Ikhlas, S. Dasgupta, F. Theuss, T. Higo, S. Kittaka, B. J. Ramshaw, O. Tchernyshyov, C. W. Hicks, and S. Nakatsuji, Nat. Phys. **18**, 1086 (2022).

[8] W. Wu and Z. L. Wang, Nat. Rev. Mater. **1**, 16031 (2016).

[9] L. Tiemann, S. Mueller, Q. S. Wu, T. Tschirky, K. Ensslin, W. Wegscheider, M. Troyer, A. A. Soluyanov, and T. Ihn, Phys. Rev. B **95**, 115108 (2017).

[10] D. Larbalestier, A. Gurevich, D. M. Feldmann, and A. Polyanskii, Nature (London) **414**, 368 (2001).

[11] P. A. Lee, N. Nagaosa, and X. G. Wen, Rev. Mod. Phys. **78**, 17 (2006).

[12] K. Ueno, S. Nakamura, H. Shimotani, A. Ohtomo, N. Kimura, T. Nojima, H. Aoki, Y. Iwasa, and M. Kawasaki, Nat. Mater. **7**, 855 (2008).

[13] A. T. Bollinger, G. Dubuis, J. Yoon, D. Pavuna, J. Misewich, and I. Božović, Nature (London) **472**, 458 (2011).

[14] J. T. Ye, S. Inoue, K. Kobayashi, Y. Kasahara, H. T. Yuan, H. Shimotani, and Y. Iwasa, Nat. Mater. **9**, 125 (2010).

[15] L. Gao, Y. Y. Xue, F. Chen, Q. Xiong, R. L. Meng, D. Ramirez, C. W. Chu, J. H. Eggert, and H. K. Mao, Phys. Rev. B **50**, 4260(R) (1994).

[16] S. Sadewasser, J. S. Schilling, A. P. Paulikas, and B. W. Veal, Phys. Rev. B **61**, 741 (2000).

[17] S. Margadonna, Y. Takabayashi, Y. Ohishi, Y. Mizuguchi, Y. Takano, T. Kagayama, T. Nakagawa, M. Takata, and K. Prassides, Phys. Rev. B **80**, 064506 (2009).

[18] J. P. Locquet, J. Perret, J. Fompeyrine, E. Mächler, J. W. Seo, and G. Van Tendeloo, Nature (London) **394**, 453 (1998).

[19] J. P. Ruf, H. Paik, N. J. Schreiber, H. P. Nair, L. Miao, J. K. Kawasaki, J. N. Nelson, B. D. Faeth, Y. Lee, B. H. Goodge, B. Pamuk, C. J. Fennie, L. F. Kourkoutis, D. G. Schlom, and K. M. Shen, Nat. Commun. **12**, 59 (2021).

[20] J. Engelmann, V. Grinenko, P. Chekhonin, W. Skrotzki, D. V. Efremov, S. Oswald, K. Iida, R. Hühne, J. Hänisch, M. Hoffmann, F. Kurth, L. Schultz, and B. Holzapfel, Nat. Commun. **4**, 2877 (2013).

[21] M. L. Lee, E. A. Fitzgerald, M. T. Bulsara, M. T. Currie, and A. Lochtefeld, J. Appl. Phys. **97**, 011101 (2005).

[22] F. Tsui, M. C. Smoak, T. K. Nath, and C. B. Eom, Appl. Phys. Lett. **76**, 2421 (2000).

[23] T. Horide, F. Kametani, Y. Yoshioka, T. Kitamura, and K. Matsumoto, ACS Nano **11**, 1780 (2017).

[24] A. F. Moreira dos Santos, A. K. Cheetham, W. Tian, X. Pan, Y. Jia, N. J. Murphy, J. Lettieri, and J. D. G. Schlom, Appl. Phys. Lett. **84**, 91 (2004).

[25] K. Osamura, S. Machiya, K. Kajiwara, T. Kawasaki, S. Harjo, Y. Zhang, S. Fujita, Y. Iijima, and D. P. Hampshire, AIP Adv. **9**, 075216 (2019).

[26] S. Awaji, T. Suzuki, H. Oguro, K. Watanabe, and K. Matsumoto, Sci. Rep. **5**, 11156 (2015).

[27] P. Giannozzi, O. Andreussi, T. Brumme, O. Bunau, M. Buongiorno Nardelli, M. Calandra, R. Car, C. Cavazzoni, D. Ceresoli, and M. Cococcioni, J. Phys.: Condens. Matter **29**, 465901/1 (2017).

[28] P. Giannozzi, S. Baroni, N. Bonini, M. Calandra, R. Car, C. Cavazzoni, D. Ceresoli, G. L. Chiarotti, M. Cococcioni, I. Dabo *et al.*, J. Phys. Condens. Matter **21**, 395502/1 (2009).

[29] M. J.van Setten, M. Giantomassi, E. Bousquet, M. J. Verstraete, D. R. Hamann, X. Gonze, and G. M. Rignanese, Comput. Phys. Commun. **226**, 39 (2018).

[30] D. R. Hamann, Phys. Rev. B **88**, 085117 (2013).

[31] J. P. Perdew, K. Burke, and M. Ernzerhof, Phys. Rev. Lett. **77**, 3865 (1996).

[32] See Supplemental Material at http://link.aps.org/supplemental/10.1103/PhysRevMaterials.8.094802 for total energy and the distance between the Cu and apex-oxygen O(A) atoms as a function of the strain; calculated band structures of La_2CuO_4; calculated Wannier orbital energies in the CuO_6 octahedron; geometry of the specimen and strain gauge and measured strain; the dependence of XRD, $\rho - T$ curve, and T_c results on the thickness and the Sr content; lattice parameter, c, and $T_c{-}c$ relationship of the LSCO films compared with the bulk LSCO; the R-T curves for the bending history including the tensile strain. It also contains Ref. [33].

[33] E. Pavarini, I. Dasgupta, T. Saha-Dasgupta, O. Jepsen, and O. K. Andersen, Phys. Rev. Lett. **87**, 047003 (2001).

[34] K. Nakamura, Y. Yoshimoto, and Y. Nomura, Comput. Phys. Commun. **261**, 10778 (2021).

[35] Y. Iijima, N. Tanabe, O. Kohno, and Y. Ikeno, Appl. Phys. Lett. **60**, 769 (1992).

[36] C. P. Wang, K. B. Do, M. R. Beasley, T. H. Geballe, and R. H. Hammond, Appl. Phys. Lett. **71**, 2955 (1997).

[37] C. C. Clickner, J. W. Ekin, N. Cheggour, C. L. H. Thieme, Y. Qiao, Y.-Y. Xie, and A. Goyal, Cryogenics **46**, 432 (2006).

[38] B. Kunert, Y. Mols, M. Baryshniskova, N. Waldron, A. Schulze, and R. Langer, Semicond. Sci. Technol. **33**, 093002 (2018).

[39] P. A. Gruber, J. Böhm, F. Onuseit, A. Wanner, R. Spolenak, and E. Arzt, Acta Mater. **56**, 2318 (2008).

[40] X. W. Liu and A. A. Hopgood, J. Appl. Phys. **128**, 125708 (2020).

[41] T. Suzuki, S. Awaji, H. Oguro, and K. Watanabe, IEEE Trans. Appl. Supercond. **25**, 8400704 (2015).

[42] H. Takagi, T. Ido, S. Ishibashi, M. Uota, S. Uchida, and Y. Tokura, Phys. Rev. B **40**, 2254 (1989).

[43] T. Horide, K. Matsumoto, P. Mele, Y. Yoshida, A. Ichinose, R. Kita, S. Horii, and M. Mukaida , Phys. Rev. B **79**, 092504 (2009).

[44] R. J. Olsson, W.-K. Kwok, L. M. Paulius, A. M. Petrean, D. J. Hofman, and G. W. Crabtree, Phys. Rev. B **65**, 104520 (2002).

[45] G. Blatter, M. V. Feigel'man, V. B. Geshkenbein, A. I. Larkin, and V. M. Vinokur, Rev. Mod. Phys. **66**, 1125 (1994).

[46] L. Benfatto, A. Toschi, S. Caprara, and C. Castellani, Phys. Rev. B **66**, 054515 (2002).

[47] M. Hashimoto, I. Vishik, R. H. He, T. P. Devereaux, and Z. X. Shen, Nat. Phys. **10**, 483 (2014).

[48] N. P. Ong, Z. Z. Wang, J. Clayhold, J. M. Tarascon, L. H. Greene, and W. R. McKinnon, Phys. Rev. B **35**, 8807(R) (1987).

[49] C. Proust and L. Taillefer, Annu. Rev. Condens. Matter Phys. **10**, 409 (2019).

[50] A. Stangl, A. Palau, G. Deutscher, X. Obradors, and T. Puig, Sci. Rep. **11**, 8176 (2021).

[51] H. Sato, A. Tsukada, M. Naito, and A. Matsuda, Phys. Rev. B **61**, 12447 (2000).

[52] I. Bozovic, G. Logvenov, I. Belca, B. Narimbetov, and I. Sveklo, Phys. Rev. Lett. **89**, 107001 (2002).

[53] M. Naito, H. Sato, A. Tsukada, and H. Yamamoto, Physica C (Amsterdam, Neth.) **546**, 84 (2018).

[54] E. M. Choi, A. D. Bernardo, B. Zhu, P. Lu, H. Alpern, K. H. L. Zhang, T. Shapira, J. Feighan, X. Sun, J. Robinson, Y. Paltiel, O. Millo, H. Wang, Q. Jia, and J. L. MacManus-Driscoll, Sci. Adv. **5**, aav5532 (2019).

[55] Y. Ohta, T. Tohyama, and S. Maekawa, Phys. Rev. B **43**, 2968 (1991).

[56] K. Momma and F. Izumi, J. Appl. Crystallogr. **44**, 1272 (2011).

[57] H. Sakakibara, H. Usui, K. Kuroki, R. Arita, and H. Aoki, Phys. Rev. Lett. **105**, 057003 (2010).